

EDGE ARTICLE

[View Article Online](#)
[View Journal](#) | [View Issue](#)Cite this: *Chem. Sci.*, 2024, **15**, 10146 All publication charges for this article have been paid for by the Royal Society of Chemistry

Elevating the upconversion performance of a multiple resonance thermally activated delayed fluorescence emitter *via* an embedded azepine approach[†]

Yi-Kuan Chen,^{‡,a} Jian Lei,^{‡,ab} and Tien-Lin Wu,^{‡,ac}

Multiple resonance thermally activated delayed fluorescence (MR-TADF) emitters hold promise for efficient organic light-emitting diodes (OLEDs) and wide gamut displays. An azepine donor is introduced into the boron–nitrogen system for the first time. The highly twisted conformation of a seven-ring embedded new molecule, **TAzBN**, increases the intermolecular distances, suppressing self-aggregation emission quenching. Meanwhile, the azepine donor is crucial to achieve a narrow singlet-triplet gap (0.03 eV) as well as boost the reverse intersystem crossing (RISC) rate to $8.50 \times 10^5 \text{ s}^{-1}$. It is noteworthy that **TAzBN** demonstrates an impressive photoluminescence quantum yield of 94%. In addition, its nonsensitized OLED displayed a remarkable external quantum efficiency (EQE_{max}) with values peaking at 27.3%, and an EQE of 21.4% at 500 cd m^{-2} . This finding shows that when **TAzBN** is used at a high concentration of 10 wt%, its device maintains efficiency even at higher brightness levels, highlighting **TAzBN**'s resistance to aggregation quenching. Furthermore, **TAzBN** enantiomers showed circularly polarized photoluminescence characteristics with dissymmetry factors $|g_{\text{PL}}|$ of up to 1.07×10^{-3} in doped films. The curved heptagonal geometry opens an avenue to design the MR-TADF emitters with fast spin-flip and chiroptical properties.

Received 9th April 2024
Accepted 22nd May 2024DOI: 10.1039/d4sc02351j
rsc.li/chemical-science

Introduction

Thermally activated delayed fluorescence (TADF) technology has become a hot topic in the field of organic light-emitting diodes (OLEDs). Especially for the newly developed multiple resonance (MR) emitters, their features of exciton up-conversion and narrow emission can meet the requirements of high-performance and high-resolution displays.^{1–4} In 2016, Hatakeyama *et al.*⁵ presented the **DABNA** series, the first MR-TADF materials. The design strategy is to utilize the opposite resonance effects of boron and nitrogen atoms to separate the highest occupied molecular orbital (HOMO) and lowest unoccupied molecular orbital (LUMO) distributions. As a result, a rigid heteroatom polyaromatic framework simultaneously exhibits TADF properties and a narrow full width at half

maximum (FWHM) of 30 nm. Recently, MR-TADF materials with five,⁶ six,^{7,8} or seven-membered⁹ rings with boron, nitrogen or oxygen atoms were developed and reported. Those state-of-the-art molecules contain high photoluminescence quantum yields (PLQYs) and a narrow emission bandwidth of around 20 nm.^{10–12} However, most MR-TADF materials display relatively wide singlet-triplet gaps (*e.g.*, $\Delta E_{\text{ST}} \geq 0.12 \text{ eV}$) due to the inherent short-range charge transfer (SRCT) of the excited state.^{13,14} Thus, reverse intersystem crossing (RISC) processes from triplet to singlet excited states in MR-TADF systems are slower than in conventional TADF emitters. And their rate constants are generally lower than 10^4 s^{-1} , resulting in serious device efficiency roll-offs at high luminance.^{15–17} So far, the design strategy for preparing MR-TADF materials with a fast triplet exciton conversion is still an enormous challenge.

Based on prior MR molecular designs, some successful strategies have emerged to enhance RISC rates (k_{RISC}) and mitigate the efficiency roll-off in OLEDs. For example, extended MR frameworks^{18–23} can effectively lower the value of ΔE_{ST} . With incorporating heavy atoms,^{24–27} MR emitters enhance the strength of spin-orbit coupling (SOC), accelerating k_{RISC} . In addition, the exciplex formation from the host and guest also boosts the TADF efficiency in MR molecules.²⁸ These above methods could expedite the spin-flip process and further reduce the efficiency roll-off in their OLEDs. However, the planar

^aDepartment of Chemistry, National Tsing Hua University, No. 101, Sec. 2, Kuang-Fu Rd., Hsinchu 300044, Taiwan. E-mail: tlwu@mx.nthu.edu.tw

^bInstitute of Atomic and Molecular Sciences, Academia Sinica, No. 1, Sec. 4, Roosevelt Rd., Taipei, 106319, Taiwan

^cCollege of Semiconductor Research, No. 101, Sec. 2, Kuang-Fu Rd., Hsinchu 300044, Taiwan

† Electronic supplementary information (ESI) available. CCDC 2347003 and 2347004. For ESI and crystallographic data in CIF or other electronic format see DOI: <https://doi.org/10.1039/d4sc02351j>

‡ These authors contributed equally.



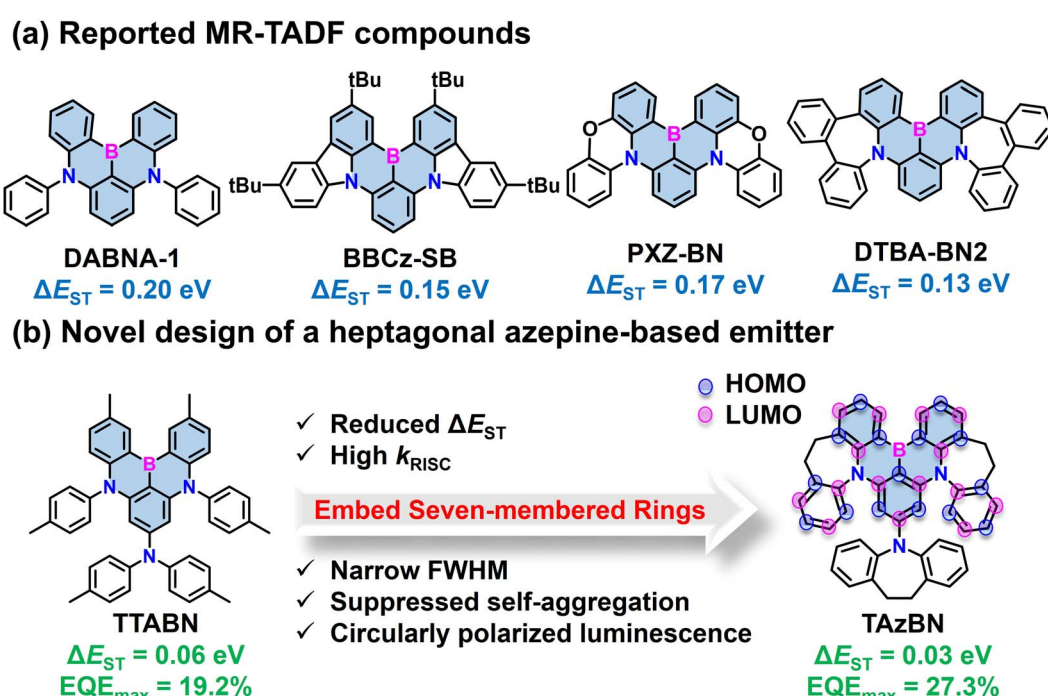
structures of most MR emitters cause strong π - π stacking interactions, resulting in serious aggregation-caused quenching (ACQ) effects and spectral broadening in the solid state. The well-known strategy is to increase the steric hindrance (*i.e.* *tert*-butyl or carbazole groups) on the peripheral side of a molecule.^{22,29-32} The bulky substituents can suppress π - π stacking interactions between planar MR cores, inhibiting the ACQ quenching. However, there is no practical way to simultaneously resolve the two issues of low up-conversion rate and aggregation quenching. Herein, we proposed a molecular design strategy with three azepine groups (Scheme 1) that concurrently decreases the singlet-triplet gap (ΔE_{ST}), increases SOC³³ and k_{RISC} , and suppresses the ACQ effect. A newly designed compound, **TAzBN**, exhibited superior photophysical properties with a PLQY (94%) and narrowband emission (FWHM of 44 nm). **TAzBN** was determined to have a low singlet-triplet difference of 0.03 eV and a high RISC rate of 8.50×10^5 s⁻¹, which revealed the efficient up-conversion pathway among reported MR-TADF emitters. Its optimized device with 10 wt% **TAzBN** showed the highest external quantum efficiency (EQE_{max}) of 27.3% and a mild efficiency roll-off of 22% at 500 nits. Moreover, **TAzBN**'s enantiomers display circularly polarized luminescence (CPL) with PL dissymmetry factors (g_{PLS}) of $+0.79 \times 10^{-3}$ / -1.07×10^{-3} for *PP*-**TAzBN** and *MM*-**TAzBN**, respectively. This work provides a novel strategy using a twisted seven-ring to design a highly efficient and narrowband emitter, which has excellent potential in CPL applications.

Results and discussion

At first, we selected a reported material with three di-*p*-tolyl amine groups, 2,12-dimethyl-*N,N*,5,9-tetra-*p*-tolyl-5,9-dihydro-

5,9-diaza-13b-boranaphtho[3,2,1-*de*]anthracen-7-amine (**TTABN**), as a model for synthesis and comparison.³⁴ Synthetic routes to the two compounds, **TTABN** and **TAzBN**, are provided in Fig. 1a, and both desired products were synthesized within two steps. In the first step, the synthesis of TAz is achieved in 83% yield *via* the Buchwald–Hartwig reaction. Then, the following direct electrophilic borylation using boron tribromide gave **TAzBN** in 23% yield at 195 °C. Because the TAz's crowded three azepine groups generate a highly congested structure, the reaction barrier of borylation might be much higher than TTA. Therefore, the borylation at 170 °C afforded **TAzBN** in an even lower yield of 11%. Characterization by ¹H/¹³C NMR, elemental analysis, high-resolution mass spectroscopy, and single-crystal X-ray diffraction is provided in the ESL.[†] Furthermore, the thermal properties are determined *via* thermal gravimetric analysis (TGA) and differential scanning calorimetry (DSC) measurements, as shown in Fig. S1.[†] They both have excellent thermal stability, and the decomposition temperatures are higher than 380 °C, respectively. The glass transition temperatures are 228 °C and 252 °C respectively for **TTABN** and **TAzBN**, implying favorable solid-state behavior during device operation. Cyclic voltammetry (CV) measurement was then carried out to estimate their frontier orbitals, highest occupied molecular orbitals (HOMO) and lowest unoccupied molecular orbitals (LUMO) levels. In Fig. S2,[†] HOMO and LUMO energy levels of **TTABN** and **TAzBN** are determined as -4.97 / -2.26 and -5.10 / -2.39 eV, respectively. As a result, they both revealed the regular electrochemical stability in the solution.

Fig. 1b and c show the X-ray single-crystal structure and analysis of **TTABN** and **TAzBN**. **TAzBN** exhibited a relatively twisted **DABNA** core (marked in blue), compared to that of **TTABN** (Tables S1 and S2[†]). The torsion angles of the triangle **DABNA** core (blue



Scheme 1 (a) Reported MR-TADF compounds. (b) Novel design of a heptagonal azepine-based emitter and its features.



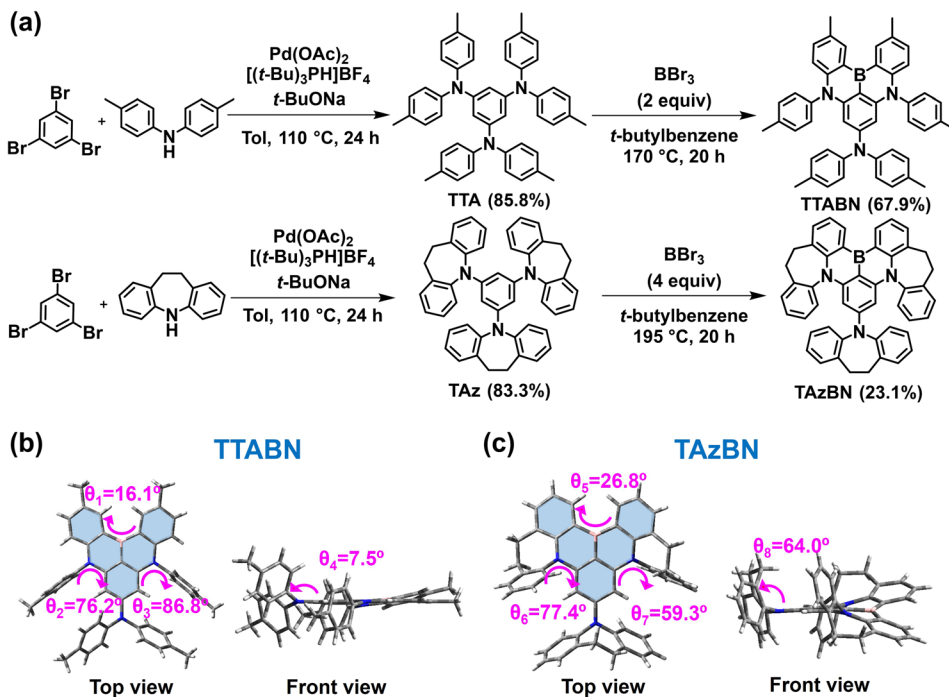


Fig. 1 (a) Synthetic routes to TTABN and TAzBN. (b) The single crystal of TTABN. (c) The single crystal of TAzBN.

region) were measured to be θ_1 of 16.1° for TTABN and θ_5 of 26.8° for TAzBN. Furthermore, we introduced the additional auxiliary azepine donor to induce steric hindrance with a relatively larger dihedral angle ($\theta_8 = 64.0^\circ$) (Fig. S3 and S4†), which might suppress the intramolecular rotational vibrations. In contrast, the auxiliary di-*p*-tolyl amine of TTABN could freely rotate, leading to a more planar structure. In Fig. S5,† there is no intense intermolecular π – π stacking interaction between TAzBN's torsional MR cores. The results revealed that intermolecular exciton distances might be effectively increased by the introduction of azepine groups, which could suppress the ACQ effect in the solid state and reduce the efficiency roll-off of OLEDs.

To investigate the effect of the introduced azepine, we carried out the density functional theory (DFT), time-dependent DFT (TD-DFT), and Tamm–Dancoff approximation DFT (TDA-DFT) calculations using the B3LYP/6-31G(d) (Fig. S6, S7 and Table S3†).^{11,35} The calculated HOMO/LUMO energy levels of TTABN and TAzBN are $-4.71/-1.25$ eV and $-4.82/-1.38$ eV, respectively. As shown in Fig. S8,† the HOMO is mainly located on the nitrogen atoms, and the LUMO is located primarily on boron atoms. According to the charge distributions in TAzBN, there are only weak conjugations between azepine units and the DABNA core. Thus, the HOMO and LUMO levels of TAzBN are deeper than those of TTABN. The TAzBN's frontier molecular orbitals (FMOs) indicate SRCT characteristics and the effectiveness of the MR feature.^{36,37} The oscillator strengths (f) of the S_1 – S_0 transition of TTABN and TAzBN are 0.2710 and 0.2395, respectively. In addition, the two emitters show small root-mean-square deviation (RMSD) values between the optimized S_1 and S_0 geometries in the solid phase (Fig. S9†). The low RMSD values and reorganization energies (λ) of TTABN and

TAzBN are 0.03/0.19 and 0.04/0.29 Å eV^{−1} in the solid phase, respectively. As a result, the simulations suggest that the molecular relaxation of TAzBN is well suppressed, and it emits narrowband blue light.

The natural transition orbitals (NTOs) of the singlet (S_1) and triplet excited states ($T_1/T_2/T_3$) and their spin–orbit couplings (SOC) are performed as shown in Fig. 2. For the first singlet and triplet excited states, NTO distributions closely resemble each other, resulting in a low SOC value between the S_1 and T_1 excited states. The values of SOCs (S_1T_1) are 0.03 and 0.08 cm^{−1} for TTABN and TAzBN, respectively. In this case, these two states S_1 and T_1 have almost identical transition orbital distributions, which hinder the RISC path from T_1 to S_1 . In contrast, the two higher triplet excited states (T_2 and T_3) of the TAzBN exhibit distinctly different NTO distribution patterns from S_1 . Interestingly, the “hole” and “electron” of TAzBN are not only distributed over the π -conjugated DABNA core but also localized on the azepine region, indicating the hybrid behavior of SRCT and long-range charge transfer (LRCT) nature.^{36,37} Thus, the values of SOC(S_1T_2) and SOC(S_1T_3) of TAzBN are 1.33 and 0.10 cm^{−1}, which are higher than those of TTABN (0.14 and 0.01 cm^{−1}). Specifically, the SOC(S_1T_2) values of the two compounds are higher than the SOC(S_1T_1) and SOC(S_1T_3) values, indicating a possible up-conversion from T_2 to S_1 state in Table S5†. A similar RISC pathway has been revealed among several MR-TADF materials,^{10,35,38} and it is expected that the higher triplet states could accelerate the overall RISC rate. Moreover, we summarize the calculated excited levels in Table S4†. The calculated $\Delta E(S_1T_2)$ values of TTABN and TAzBN are 0.09 and 0.02 eV in toluene, and 0.10 and 0.01 eV in the solid

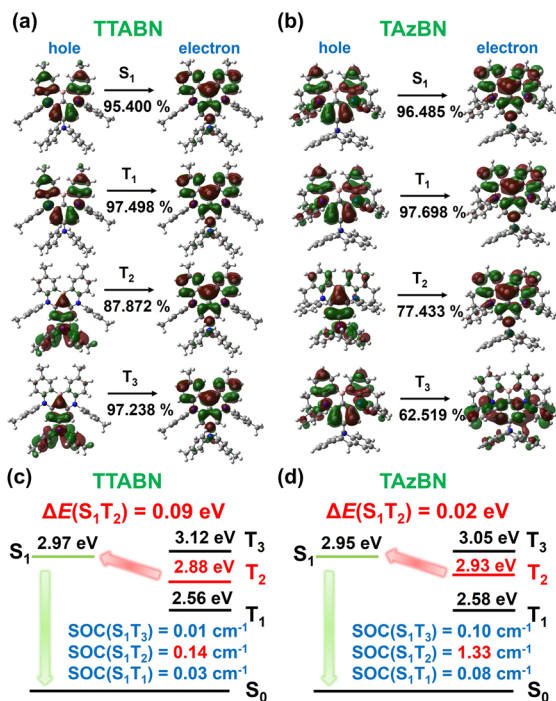


Fig. 2 Calculated natural transition orbitals (NTOs) based on the optimized S_0 geometries, adiabatic excited state energies, and associated SOC matrix elements based on the optimized S_1 geometries for (a and c) TTABN and (b and d) TAzBN, respectively, in toluene by TDA-DFT at the B3LYP/6-31G(d) level.

phase, respectively, implying the possible path of an efficient RISC process.

The ultraviolet-visible (UV-vis) absorption and photoluminescence (PL) spectra of TTABN and TAzBN were measured in toluene (1×10^{-5} M). As shown in Fig. 3a and b, strong absorption bands originating from HOMO-LUMO transitions were observed at 439 and 433 nm for TTABN and TAzBN, respectively. The intramolecular charge transfer (ICT) characteristics were confirmed by emission spectra in various solvents in Fig. S10.[†] TAzBN's red-shifted and broadened bands reveal a slightly stronger ICT effect than TTABN, possibly due to the auxiliary azepine. Both PL spectra of TTABN and TAzBN display narrow bandwidth emissions at 459 and 464 nm, respectively, which agrees with the TD-DFT calculations (Fig. S11[†]). Notably, the Stokes shifts of TTABN and TAzBN are 19 and 32 nm, and the full-width at half-maximum (FWHM) values of TTABN and TAzBN PL bands are 21 and 35 nm, respectively. In Fig. 3c and d, we further measured the fluorescence and phosphorescence spectra of 2 wt% emitters doped in a 9-(3-(9H-carbazol-9-yl)phenyl)-9H-carbazole-3-carbonitrile (mCPCN) host. The experimental ΔE_{ST} values of TTABN and TAzBN are determined as 60 and 32 meV, respectively. Especially for the low gap of TAzBN, it is the lowest value among reported MR-TADF molecules. The results are consistent with the trend of theoretical calculations and imply the participation of higher triplet states.^{3,38,39} The summary of photophysical data is listed in Table 1.

The transient PL measurements for the two materials in doped films were performed to investigate the features of TADF

(Fig. 4, S12 and S13[†]). In Fig. 4a and b, the delayed fluorescence component increases along with the rising temperature, which strongly supports the TADF mechanism. The prompt and delayed lifetimes (τ_p and τ_d) were determined by fitting the decay curves of 300 K. The delayed fluorescence decay curves of TTABN and TAzBN-based films were analyzed and fitted. The methods and results of the fitting process are illustrated in Fig. S12 and S13.[†] Further details are provided in the ESI.[†] As shown in the results, the τ_p values of TTABN and TAzBN were 8.3 and 9.2 ns, indicating that the twisted structure of TAzBN still retains the LE feature of fast decay. Moreover, TAzBN has a much lower τ_d of 15.8 μ s, compared to that of TTABN (65.5 μ s). The trend of delayed components of the two emitters is highly correlated with their ΔE_{ST} values (Fig. S14[†]). Next, we investigated the concentration effect of the emitters in the solid phase, and vacuum-evaporated films with 2, 10, and 30 wt% doping concentrations were prepared for the transient PL and PLQY measurements. The decay curves of TAzBN at various concentrations exhibit relatively minor differences compared to the results of TTABN, as shown in Fig. 4c and d. This indicates a high consistency in the fluorescence behavior of TAzBN with increasing concentration. For the low-doped concentration films (2 wt% in mCPCN), TTABN and TAzBN showed high PLQYs (higher than 90%), compared to those of only 39% (TTABN) and 25% (TAzBN) in degassed toluene. Such high values in doped films indicate efficient energy transfer from the host and superior emission behaviors of the organoboron emitters. For 10 wt% doping films, the PLQY value of TAzBN significantly increased to 94%. However, that of TTABN dropped to 65%, revealing the serious emission quenching caused by aggregation. Moreover, the k_{RISC} of TAzBN (8.50×10^5 s⁻¹) is much higher than that of TTABN (4.79×10^4 s⁻¹). Compared with planar TTABN, such an efficient up-conversion behavior of TAzBN could be attributed to the reduced ΔE_{ST} and strong spin-orbital coupling *via* the introduction of the twisted heptagonal azepine. Furthermore, the PLQY of the 30 wt% TAzBN doped film remained 90%, and its k_{RISC} reached 4.83×10^5 s⁻¹. Importantly, it is one of the highest k_{RISC} values among blue MR-TADF emitters, even without heavy atoms or assisted sensitizers. The corresponding PL properties are summarized in Table S6[†]. Due to the high k_{RISC} and slightly reduced PLQY under high doping concentrations, we believe that the extensively twisted molecular configurations and the fast spin-flip process of TAzBN play a role in inhibiting the ACQ effect and non-radiative transition. The advantages of TAzBN in singlet and triplet exciton conversion could benefit the luminous efficiency of OLEDs and alleviate the decay of efficiency at high brightness.

Furthermore, we notice the helical structure of TAzBN from its single crystal, which results in enantiomers. To investigate the chiroptical properties, we measured circular dichroism (CD) and circularly polarized photoluminescence (CPL) spectra for thin films (Fig. 5). As shown in Fig. 5b, mirror-image CD signals are observed for *PP*-TAzBN and *MM*-TAzBN with an obvious cotton effect in the $n-\pi^*/\pi-\pi^*$ region from 350 to 450 nm. The CPL spectra of *PP*-TAzBN and *MM*-TAzBN enantiomers are symmetrical in their co-doped films (Fig. 5d), reflecting the



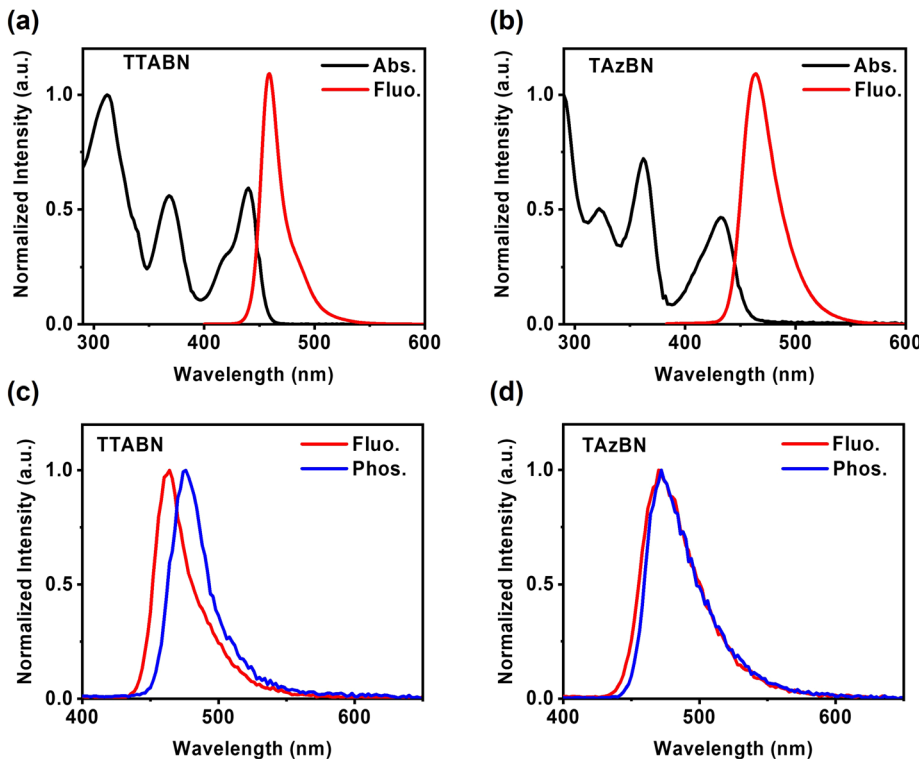


Fig. 3 Absorption and fluorescence spectra of (a) TTABN and (b) TAzBN were measured at 300 K in toluene. Fluorescence (300 K) and phosphorescence (77 K, delayed time: 6.25 ms) spectra of (c) TTABN and (d) TAzBN measured in doped films (2 wt% in mCPCN).

Table 1 Photophysical properties of TTABN and TAzBN

| Emitter | $\lambda_{\text{Abs},\text{max}}^a$ [nm] | $\lambda_{\text{PL},\text{max}}^a$ [nm] | FWHM ^b [nm] | HOMO ^c [eV] | LUMO ^d [eV] | T_d/T_g^d (°C) | S_1/T_1^e [eV] | ΔE_{ST}^e [meV] | τ_p^f [ns] | τ_d^f [μs] |
|---------|--|---|------------------------|------------------------|------------------------|------------------|------------------|--------------------------------|-----------------|-----------------|
| TTABN | 312 440 | 459 | 21 | -4.97 | -2.26 | 381/228 | 2.80/2.74 | 60 | 8.3 | 65.5 |
| TAzBN | 290 432 | 464 | 35 | -5.10 | -2.39 | 400/252 | 2.79/2.76 | 32 | 9.2 | 15.8 |

^a Absorption and photoluminescence spectra measured in toluene (1.0×10^{-5} M) at 300 K. ^b FWHM of PL bands in toluene. ^c The HOMO level was determined from the CV, LUMO = HOMO + E_g . ^d T_d as decomposition temperature (5% weight loss) and T_g as glass transition temperature. ^e S_1 and T_1 were determined by analyzing the onset of the fluorescence band (at 300 K) and phosphorescence band (at 77 K) in thin films (2 wt% compound doped in mCPCN); $\Delta E_{\text{ST}} = S_1 - T_1$. ^f Fluorescence lifetimes of the prompt part (τ_p) and delayed part (τ_d) in doped mCPCN films (2 wt% doping ratio); $\sum B_i \tau_i^2$

The average lifetime was calculated according to the equation: $\tau_{\text{average}} = \frac{\sum_i B_i \tau_i}{\sum_i B_i \tau_i^2}$, where B_i is the pre-exponential for lifetime τ_i .⁴⁰⁻⁴²

chirality of the singlet excited state. Notably, the photoluminescence dissymmetry factors (g_{PL}) of *PP*-TAzBN and *MM*-TAzBN were determined as $+0.79 \times 10^{-3}$ and -1.07×10^{-3} . To discuss the relationship between the chiral structure and CPL properties of the emitter, relative calculations were performed to analyze the dissymmetry factor (Fig. S15, S16 and Table S7†). The PL dissymmetry factor is described as eqn (1):⁴³

$$g_{\text{PL}} = \frac{4|\mu||m| \cos \theta_{\mu,m}}{|\mu|^2 + |m|^2} \quad (1)$$

μ , m and $\theta_{\mu,m}$ are the transition electric dipole moment, magnetic dipole moment, and their angle respectively. Obviously, $|\mu|$, $|m|$, and $\cos \theta_{\mu,m}$ are the three key parameters for evaluating the g_{PL} . The simulated g_{PL} values of *PP/MM*-TAzBN

are $+2.26 \times 10^{-3}$ / -2.26×10^{-3} in the solid phase, respectively, which are consistent with the experimental results. Overall, the strategy of the embedded heptagonal ring achieves a novel MR-TADF emitter, TAzBN, with efficient TADF, reduced ACQ, and chiroptical features.

Next, we proceeded to create a series of OLEDs, utilizing the two compounds as emitters, with a device configuration of ITO (indium tin oxide)/MoO₃ (1 nm)/TAPC (*N,N*-bis(*p*-tolyl)aniline) (50 nm)/mCP (1,3-di(*9H*-carbazol-9-yl)benzene) (10 nm)/mCPCN: 2–50 wt% emitters (20 nm)/tris-[3-(3-pyridyl)mesityl] borane (3TPYMB) (50 nm)/LiF (0.5 nm)/Al (100 nm) (see Fig. 6a). mCPCN was chosen as the host material due to its high T_1 state (2.96 eV) and balanced bipolar carrier transport capability. Indium tin oxide (ITO) and Al are the anode and cathode, respectively. Di-[4-(*N,N*-ditolyl-amino)-phenyl]-cyclohexane

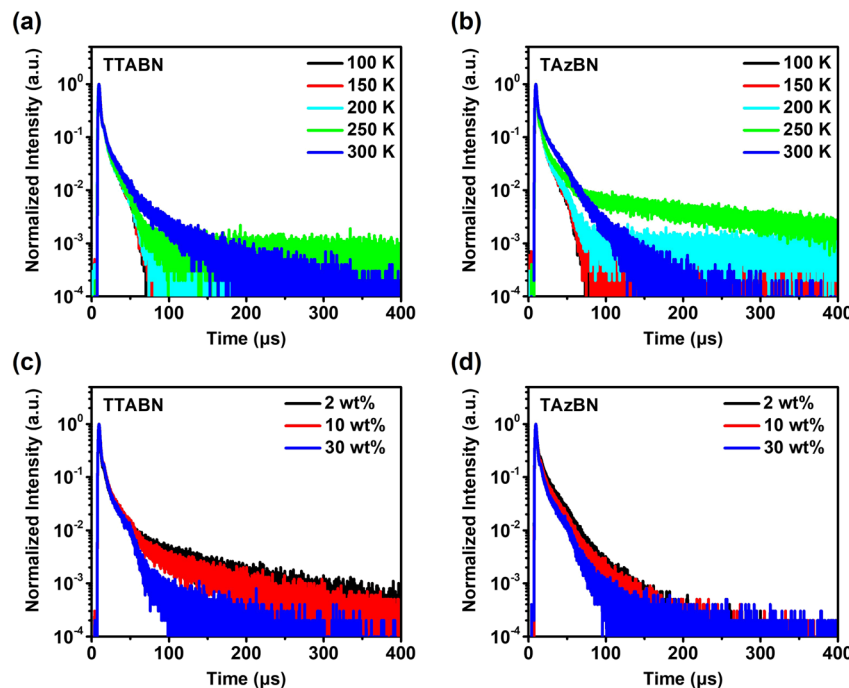


Fig. 4 Temperature-dependent transient PL characteristics in doped films (2 wt% in mCPCN) for (a) TTABN and (b) TAzBN. Transient PL characteristics of (c) TTABN and (d) TAzBN with dopant concentrations of 2 to 30 wt% in the mCPCN host.

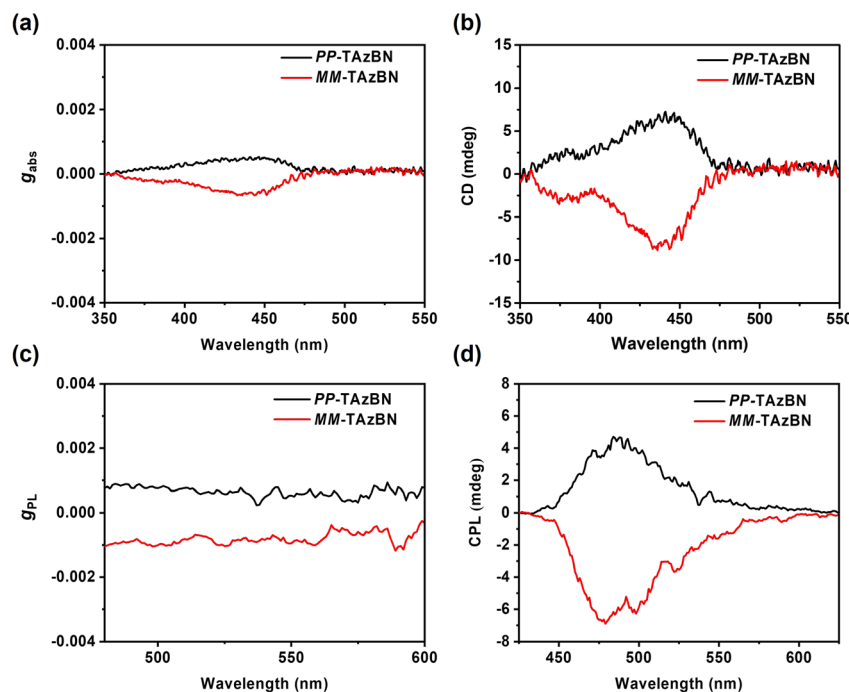


Fig. 5 (a) Absorption dissymmetry factor (g_{abs}) and (b) circular dichroism (CD) spectra of TAzBN in doped films (2 wt% in mCPCN). (c) PL dissymmetry factor (g_{PL}) and (d) circularly polarized photoluminescence (CPL) spectra of TAzBN in doped films (2 wt% in mCPCN).

(TAPC) and *N,N*-dicarbazolyl-3,5-benzene (mCP) are hole-transport layers (HTL). The mCPCN host with each dopant emitter is composed of the emitting layer (EML). 3TPYMB is the electron-transport layer (ETL). MoO₃ and LiF are the hole-injection and electron-injection layers, respectively. The

chemical structures of the utilized materials for OLED fabrication are depicted in Fig. 6b. The corresponding EL characteristics of OLED devices are summarized in Table S8[†] and Fig. S17.[†] In Fig. 6c and d, the TAzBN-based device (2 wt%) displayed the performance with an EL_{max} of 475 nm, EQE_{max} of



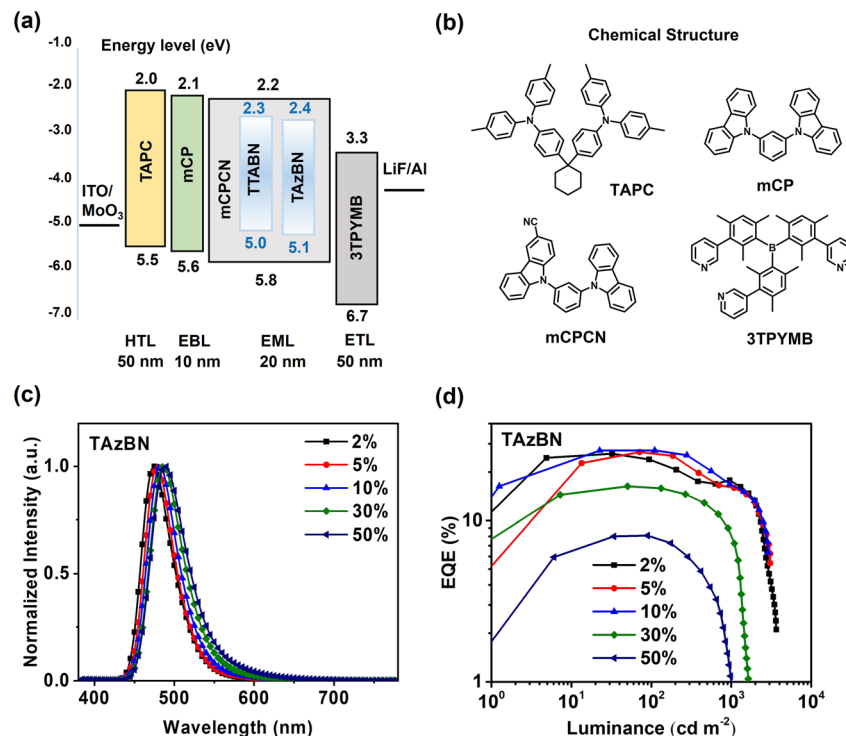


Fig. 6 Electroluminescence characteristics of blue OLEDs. (a) Device configuration and energy levels of TTABN and TAzBN. (b) The molecular structures of materials used in the devices. (c) Electroluminescence (EL) spectra of TAzBN, (d) EQE versus luminescence of TAzBN with different dopant concentrations of 2–50 wt% in the mCPCN host.

26.0%, and EQE₅₀₀ of 17.2%. Compared with TAzBN-based devices, a TTABN-based device with the same doping ratio exhibited an EL_{max} of 464 nm and EQE_{max} of 19.2%. However, its EQE₅₀₀ quickly dropped to 8.4% due to the relatively slow RISC process of TTABN. (Fig. S18†). Furthermore, nearly ideal Lambertian distributions were determined for both 2 wt%-based devices, as shown in Fig. S19.† The FWHM values of TTABN and TAzBN-based (2 wt%) devices are 31 and 45 nm, respectively. TAzBN exhibited a broader bandwidth than that of TTABN due to the twisted structure. Moving forward, we will emphasize the importance of mitigating this adverse effect, such as by introducing suitable functional groups,⁴⁴ deuteration,⁴⁵ hyper-fluorescence systems,³⁷ etc.

To study the behavior of emission quenching under electrical excitation, OLEDs with various doping ratios of EML were fabricated and measured, and the results are summarized in Table S8†. We observed that the major bands of EL spectra were slightly broadened in TAzBN-based devices. Notably, the device with a high doping (10 wt%) of TAzBN demonstrated EQE_{max} and EQE₅₀₀ values of 27.3% and 21.4%, respectively. Even at 1000 cd m⁻², the EQE remains at 16.6%, which is quite outstanding compared to most reported nonsensitized MR-TADF OLEDs, as summarized in Table S9†. TAzBN-based devices exhibited the resistance of aggregation-quenching and alleviated efficiency roll-off. In addition, the driving voltage decreased from 3.3 V to 2.6 V along with increasing concentrations. The fast RISC and the steric hindrance from the twisted azepine motif could reduce the triplet-triplet

annihilation (TTA) or triplet-polaron annihilation (TPA). It is worth noting that the device with 30 wt% TAzBN still maintained 16.3% EQE. Such high concentration of emitting layer among reported MR-TADF OLEDs is rare, and the performance of OLEDs with a high doping of TAzBN is excellent among most MR-TADF OLEDs (Fig. S20†). The result implies the successful approach to improving SOC, accelerating RISC, and further reducing ACQ *via* the molecular design of introduced heptagonal geometry.

Conclusions

In summary, we have developed a molecular design to enhance *k*_{RISC} values and suppress the ACQ effect in MR-TADF emitters. A newly developed emitter containing heptagonal rings, TAzBN, shows a narrow FWHM of 45 nm, a low ΔE_{ST} of 0.03 eV, a high PLQY of over 90%, and a high *k*_{RISC} of 8.50×10^5 s⁻¹ in doped films. Introducing the emitter as a dopant in OLEDs led to remarkable enhancements in EL performance, achieving high efficiency and reduced efficiency roll-off (EQE_{max} = 27.3%; EQE₅₀₀ = 21.4%) at a high doping ratio of 10 wt%. Moreover, the azepine-induced helical structure can show distinct CPL signals with *g*_{PLS} of $+0.79 \times 10^{-3}$ for PP-TAzBN and -1.07×10^{-3} for MM-TAzBN. The strategy of the twisted heptagonal geometry opens the avenue to solve the issues of the slow RISC process among recent MR-TADF studies. The results showcase the promising application of this strategy in constructing efficient and chiral MR-TADF emitters.

Data availability

The theoretical calculation, experimental procedure, and device fabrication details have been provided within the manuscript and ESI.† The data that support the findings of this study are available from the corresponding authors upon reasonable request.

Author contributions

Y.-K. Chen: synthesis, measurement of photophysical properties, and device fabrication; J. Lei: theoretical calculation and writing – original draft; T.-L. Wu: supervision, writing – review and editing.

Conflicts of interest

There are no conflicts to declare.

Acknowledgements

We thank the National Science and Technology Council of Taiwan (NSTC 110-2113-M-007-028-MY3). The authors acknowledge Prof. Liang-Yan Hsu for providing the supercomputing system at the Institute of Atomic and Molecular Sciences, Academia Sinica. We appreciate the support of chi-optical measurement by Prof. Yu-Chiang Chao at National Taiwan Normal University, Department of Physics. T.-L.W. acknowledges the support of the Yushan Young Scholar Program by the Ministry of Education, Taiwan.

Notes and references

- 1 A. Pershin, D. Hall, V. Lemaur, J.-C. Sancho-Garcia, L. Muccioli, E. Zysman-Colman, D. Beljonne and Y. Olivier, *Nat. Commun.*, 2019, **10**, 597.
- 2 Y. C. Cheng, X. C. Fan, F. Huang, X. Xiong, J. Yu, K. Wang, C. S. Lee and X. H. Zhang, *Angew. Chem., Int. Ed.*, 2022, **134**, e202212575.
- 3 H. J. Cheon, S. J. Woo, S. H. Baek, J. H. Lee and Y. H. Kim, *Adv. Mater.*, 2022, **34**, 2207416.
- 4 M. Yang, I. S. Park and T. Yasuda, *J. Am. Chem. Soc.*, 2020, **142**, 19468–19472.
- 5 T. Hatakeyama, K. Shiren, K. Nakajima, S. Nomura, S. Nakatsuka, K. Kinoshita, J. Ni, Y. Ono and T. Ikuta, *Adv. Mater.*, 2016, **28**, 2777–2781.
- 6 Y. Zhang, D. Zhang, J. Wei, Z. Liu, Y. Lu and L. Duan, *Angew. Chem., Int. Ed.*, 2019, **58**, 16912–16917.
- 7 G. Liu, H. Sasabe, K. Kumada, A. Matsunaga, H. Katagiri and J. Kido, *J. Mater. Chem. C*, 2021, **9**, 8308–8313.
- 8 X. Wu, J. W. Huang, B. K. Su, S. Wang, L. Yuan, W. Q. Zheng, H. Zhang, Y. X. Zheng, W. Zhu and P. T. Chou, *Adv. Mater.*, 2022, **34**, 2105080.
- 9 B. Lei, Z. Huang, S. Li, J. Liu, Z. Bin and J. You, *Angew. Chem., Int. Ed.*, 2023, **135**, e202218405.
- 10 H. Tanaka, S. Oda, G. Ricci, H. Gotoh, K. Tabata, R. Kawasumi, D. Beljonne, Y. Olivier and T. Hatakeyama, *Angew. Chem., Int. Ed.*, 2021, **60**, 17910–17914.
- 11 K. R. Naveen, J. H. Oh, H. S. Lee and J. H. Kwon, *Angew. Chem., Int. Ed.*, 2023, **62**, e202306768.
- 12 X. Cai, J. Xue, C. Li, B. Liang, A. Ying, Y. Tan, S. Gong and Y. Wang, *Angew. Chem., Int. Ed.*, 2022, **61**, e202200337.
- 13 H. J. Kim and T. Yasuda, *Adv. Opt. Mater.*, 2022, **10**, 2201714.
- 14 Y. J. Yu, Z. Q. Feng, X. Y. Meng, L. Chen, F. M. Liu, S. Y. Yang, D. Y. Zhou, L. S. Liao and Z. Q. Jiang, *Angew. Chem., Int. Ed.*, 2023, **135**, e202310047.
- 15 Y. Zhang, J. Wei, D. Zhang, C. Yin, G. Li, Z. Liu, X. Jia, J. Qiao and L. Duan, *Angew. Chem., Int. Ed.*, 2022, **61**, e202113206.
- 16 P. Jiang, J. Miao, X. Cao, H. Xia, K. Pan, T. Hua, X. Lv, Z. Huang, Y. Zou and C. Yang, *Adv. Mater.*, 2022, **34**, 2106954.
- 17 S. Madayanad Suresh, L. Zhang, D. Hall, C. Si, G. Ricci, T. Matulaitis, A. M. Slawin, S. Warriner, Y. Olivier and I. D. Samuel, *Angew. Chem., Int. Ed.*, 2023, **135**, e202215522.
- 18 P. Jiang, L. Zhan, X. Cao, X. Lv, S. Gong, Z. Chen, C. Zhou, Z. Huang, F. Ni and Y. Zou, *Adv. Opt. Mater.*, 2021, **9**, 2100825.
- 19 F. Huang, X. C. Fan, Y. C. Cheng, H. Wu, X. Xiong, J. Yu, K. Wang and X. H. Zhang, *Angew. Chem., Int. Ed.*, 2023, **135**, e202306413.
- 20 S. Oda, B. Kawakami, Y. Yamasaki, R. Matsumoto, M. Yoshioka, D. Fukushima, S. Nakatsuka and T. Hatakeyama, *J. Am. Chem. Soc.*, 2021, **144**, 106–112.
- 21 H. Jiang, J. Jin and W. Y. Wong, *Adv. Funct. Mater.*, 2023, **33**, 2306880.
- 22 K. Zhang, X. Wang, Y. Chang, Y. Wu, S. Wang and L. Wang, *Angew. Chem., Int. Ed.*, 2023, **135**, e202313084.
- 23 K. R. Naveen, H. Lee, R. Braventh, K. J. Yang, S. J. Hwang and J. H. Kwon, *Chem. Eng. J.*, 2022, **432**, 134381.
- 24 Y. Lee and J.-I. Hong, *J. Mater. Chem. C*, 2022, **10**, 11855–11861.
- 25 T. Hua, J. Miao, H. Xia, Z. Huang, X. Cao, N. Li and C. Yang, *Adv. Funct. Mater.*, 2022, **32**, 2201032.
- 26 X. Cao, K. Pan, J. Miao, X. Lv, Z. Huang, F. Ni, X. Yin, Y. Wei and C. Yang, *J. Am. Chem. Soc.*, 2022, **144**, 22976–22984.
- 27 M. Nagata, H. Min, E. Watanabe, H. Fukumoto, Y. Mizuhata, N. Tokitoh, T. Agou and T. Yasuda, *Angew. Chem., Int. Ed.*, 2021, **133**, 20442–20447.
- 28 X. Wu, B.-K. Su, D.-G. Chen, D. Liu, C.-C. Wu, Z.-X. Huang, T.-C. Lin, C.-H. Wu, M. Zhu and E. Y. Li, *Nat. Photonics*, 2021, **15**, 780–786.
- 29 K. R. Naveen, H. Lee, L. H. Seung, Y. H. Jung, C. K. Prabhu, S. Muruganantham and J. H. Kwon, *Chem. Eng. J.*, 2023, **451**, 138498.
- 30 X. Liang, Z. P. Yan, H. B. Han, Z. G. Wu, Y. X. Zheng, H. Meng, J. L. Zuo and W. Huang, *Angew. Chem., Int. Ed.*, 2018, **130**, 11486–11490.
- 31 T.-L. Wu, J. Lei, C.-M. Hsieh, Y.-K. Chen, P.-Y. Huang, P.-T. Lai, T.-Y. Chou, W.-C. Lin, W. Chen and C.-H. Yu, *Chem. Sci.*, 2022, **13**, 12996–13005.
- 32 H. Mubarok, A. Amin, T. Lee, J. Jung, J. H. Lee and M. H. Lee, *Angew. Chem., Int. Ed.*, 2023, **135**, e202306879.



33 J. E. Adams, W. Mantulin and J. R. Huber, *J. Am. Chem. Soc.*, 1973, **95**, 5477–5481.

34 S. Oda, W. Kumano, T. Hama, R. Kawasumi, K. Yoshiura and T. Hatakeyama, *Angew. Chem., Int. Ed.*, 2021, **133**, 2918–2922.

35 X. Lv, J. Miao, M. Liu, Q. Peng, C. Zhong, Y. Hu, X. Cao, H. Wu, Y. Yang and C. Zhou, *Angew. Chem., Int. Ed.*, 2022, **134**, e202201588.

36 F. Huang, X. C. Fan, Y. C. Cheng, Y. Xie, S. Luo, T. Zhang, H. Wu, X. Xiong, J. Yu and D. D. Zhang, *Adv. Opt. Mater.*, 2023, **11**, 2202950.

37 G. Meng, H. Dai, Q. Wang, J. Zhou, T. Fan, X. Zeng, X. Wang, Y. Zhang, D. Yang and D. Ma, *Nat. Commun.*, 2023, **14**, 2394.

38 K. Stavrou, A. Danos, T. Hama, T. Hatakeyama and A. Monkman, *ACS Appl. Mater. Interfaces*, 2021, **13**, 8643–8655.

39 K. Shizu and H. Kaji, *Commun. Chem.*, 2022, **5**, 53.

40 Q. Zhang, B. Li, S. Huang, H. Nomura, H. Tanaka and C. Adachi, *Nat. Photonics*, 2014, **8**, 326–332.

41 Q. Zhang, H. Kuwabara, W. J. Potsavage Jr, S. Huang, Y. Hatae, T. Shibata and C. Adachi, *J. Am. Chem. Soc.*, 2014, **136**, 18070–18081.

42 T.-L. Wu, M.-J. Huang, C.-C. Lin, P.-Y. Huang, T.-Y. Chou, R.-W. Chen-Cheng, H.-W. Lin, R.-S. Liu and C.-H. Cheng, *Nat. Photonics*, 2018, **12**, 235–240.

43 J. Lei, T. A. Lou, C. R. Chen, C. H. Chuang, H. Y. Liu, L. Y. Hsu, Y. C. Chao and T. L. Wu, *Chem.-Asian J.*, 2024, **19**, e202300940.

44 J. Liu, Y. Zhu, T. Tsuboi, C. Deng, W. Lou, D. Wang, T. Liu and Q. Zhang, *Nat. Commun.*, 2022, **13**, 4876.

45 T. Huang, Q. Wang, H. Zhang, Y. Zhang, G. Zhan, D. Zhang and L. Duan, *Nat. Photonics*, 2024, **18**, 516–523.

